

DSMC and Navier-Stokes Predictions for Hypersonic Laminar Interacting Flows

Christopher J. Roy,[†] Timothy J. Bartel,[‡] Michael A. Gallis,[§] and Jeffrey L. Payne[#]

Sandia National Laboratories^{*}

P. O. Box 5800

Albuquerque, NM 87185

Abstract

Direct Simulation Monte Carlo (DSMC) and Navier-Stokes calculations are performed for a Mach 11 25 deg.-55 deg. spherically blunted biconic. The conditions are such that the flow is laminar, with separation occurring at the cone-cone juncture. The simulations account for thermochemical nonequilibrium based on standard Arrhenius chemical rates for nitrogen dissociation and Millikan and White vibrational relaxation. The simulation error for the Navier-Stokes (NS) code is estimated to be 2% for the surface pressure and 10% for the surface heat flux. The grid spacing for the DSMC simulations was adjusted to be less than the local mean-free-path (mfp) and the time step less than the cell transient time of a computational particle. There was overall good agreement between the two simulations; however, the recirculation zone was computed to be larger for the NS simulation. A sensitivity study is performed to examine the effects of experimental uncertainty in the freestream properties on the surface pressure and heat flux distributions. The surface quantities are found to be extremely sensitive to the vibrational excitation state of the gas at the test section, with differences of 25% found in the surface pressure and 25%-35% for the surface heat flux. These calculations are part of a blind validation comparison and thus the experimental data have not yet been released.

[†] Senior Member of Technical Staff, MS 0835, E-mail: cjroy@sandia.gov, Member AIAA

[‡] Principal Member of Technical Staff, MS 0826, E-mail: tjbar-te@sandia.gov, Member AIAA

[§] Member of Technical Staff, MS 0826, E-mail: magalli@sandia.gov, Member AIAA

[#] Principal Member of Technical Staff, MS 0825, E-mail: jl-payne@sandia.gov, Member AIAA

^{*} Sandia is a multiprogram laboratory operated by Sandia Corporation, a Lockheed Martin Company, for the United States Department of Energy under Contract DE-AC04-94AL85000.

This paper is declared a work of the U. S. Government and is not subject to copyright protection in the United States.

Nomenclature

c_p	specific heat at constant pressure, J/kgK
f	general solution variable
H_o	stagnation or total enthalpy, J/kg
h	specific enthalpy, J/kg
p	pressure, N/m^2
q	heat flux, W/m^2
R	specific gas constant, J/kgK (296. for N_2)
s	specific entropy, J/kgK
T	translational temperature, K
T_r	rotational temperature, K
T_v	vibrational temperature, K
t	time, s
V	velocity magnitude, m/s
x	axial coordinate, m
y	radial coordinate, m
γ	ratio of specific heats
μ	absolute viscosity, Ns/m^2
ρ	density, kg/m^3

Subscripts

k	mesh level
RE	Richardson Extrapolation value
ref	reference value
w	wall value
∞	freestream value

Introduction

A great deal of effort is being spent validating simulation codes used for the design, analysis, and certification of engineering systems. Validation, as defined in Ref. 1, is “the process of determining the degree to which a model is an accurate representation of the real world from the perspective of the intended uses of the model.” Validation addresses the question of whether or not the proper equations have been chosen. In the area

of fluid dynamics, one can talk of validating turbulence models, chemistry models, or even of validating simulation codes themselves, for a given range of conditions.

In order to validate a model or simulation code, experimental data must be used to gauge the accuracy of the model for the conditions of interest. It is important to draw a distinction between model validation and calibration. The former must necessarily be a blind comparison so as to be a true prediction, while in the latter, the data is used to “tune” model parameters until the best agreement is found. The simulations presented in this paper were performed without prior access to the experimental data.

The experiment of interest is the Mach 11 laminar flow of nitrogen over a blunted 25 deg.-55 deg. biconic.² A large separated region exists near the 25 deg.-55 deg. juncture; however, significant regions of attached flow are present both upstream and downstream of the separated region. Prior Navier-Stokes simulations³ indicate that the flowfield is quite sensitive to the grid spacing and may even contain some unsteadiness in the separated region.

Two simulation approaches were chosen to examine the previously described experiment, Direct Simulation Monte Carlo (DSMC) and Navier-Stokes (NS). The DSMC method is a well-established technique for simulating gas flows in which mean-free-path effects are significant. The particular DSMC method used in this study is that of Bird,⁴ the massively parallel processor implementation, Icarus, is described by Bartel et al.⁵ The Navier-Stokes code employed herein is SACCARA, the Sandia Advanced Code for Compressible Aerothermodynamics Research and Analysis. The SACCARA code was developed from a parallel distributed memory version^{6,7} of the INCA code,⁸ originally written by Amtec Engineering. This code has been developed to provide a massively parallel, three-dimensional compressible fluid mechanics/aerothermodynamics analysis capability for subsonic through hypersonic flows.

The remainder of this paper is organized as follows. In the first section, the simulation approaches are described in detail. Then the computational submodels are described, including thermodynamic models, transport models, and thermochemical nonequilibrium models. In the next section, flowfield conditions and solution procedures are described, followed by a discussion of the accuracy of the simulations. Results are then presented for surface pressure and heat flux using the baseline freestream conditions. Following the results section is a sensitivity study where the freestream conditions are varied within the range of experimental uncertainty. The conclusions of this study are presented in the final section.

Simulation Approaches

Direct Simulation Monte Carlo (DSMC)

In brief, the DSMC method is applied as follows. The computational domain is populated with “computational molecules,” each of which typically represents a large number of identical real molecules (e.g., 10^{10}). During one time step, computational molecules move from one location to another, interact with boundaries, experience collisions, and are sampled to accumulate statistics. During a move, computational molecules travel at constant velocity for the entire time step or until a boundary is encountered. In the latter situation, the appropriate boundary condition is applied. Typical boundary conditions are “inflow” (computational molecules enter the domain with a prescribed Maxwellian distribution), “outflow” (computational molecules crossing this boundary are deleted, appropriate for supersonic applications), “diffuse wall” (computational molecules are reflected with a prescribed Maxwellian distribution), and “specular wall” (computational molecules are reflected with mirror symmetry). Following movement and boundary interactions, computational molecules experience collisions, which change their velocities. It should be noted that computational molecules have three-dimensional velocity vectors for collision purposes even if a two-dimensional geometry is considered. After the collision phase, statistics (e.g., number density, velocity, and temperature) are accumulated on the computational mesh, which exists only for this purpose and for determining possible collision pairs. To preclude nonphysical behavior, the mesh cells are constrained to be well less than a mean free path or a local flow gradient, and the time step is similarly constrained to less than a mean collision time.⁴

The Icarus DSMC code was written for the massively parallel computing environment to overcome the extreme computational requirements of the DSMC method.⁵ The simulations in the present work were performed on an 128 node (512 processor) IBM SP-2 computer.

Navier-Stokes

The SACCARA code is used to solve the Navier-Stokes equations for conservation of mass, momentum, and energy in axisymmetric form. The governing equations are discretized using a cell-centered finite-volume approach. The convective fluxes at the interface are calculated using the Steger-Warming⁹ flux vector splitting scheme. Second-order reconstructions of the interface fluxes are obtained via MUSCL extrapolation.¹⁰ A flux limiter is employed which reduces to first order in regions of large second derivatives of pressure and tem-

perature. This limiting is used to prevent oscillations in the flow properties at shock discontinuities. The viscous terms are discretized using central differences.

The SACCARA code employs a massively parallel distributed memory architecture based on multi-block structured grids. The solver is a Lower-Upper Symmetric Gauss-Seidel scheme based on the works of Yoon et al.^{11,12} and Peery and Imlay,¹³ which provides for excellent scalability up to thousands of processors.¹⁴ The SACCARA code has been used to obtain solutions for a wide variety of compressible flow problems.^{6,15-19} The Navier-Stokes simulations presented herein were run using a single 400 MHz processor of a Sun Enterprise 10000 shared-memory machine.

Computational Submodels

Thermodynamic Model (Navier-Stokes Only)

The non-dimensional specific heat (Cp/R), enthalpy (h/RT), and entropy (s/R) for both N and N_2 are determined via polynomial functions of the translational temperature (see Ref. 20). These curve fits are for two ranges, 300 K to 1000 K and 1000 K to 6000 K. Below 300 K, the specific heat is held constant at the value at 300 K, and the enthalpy and entropy are determined appropriately.

Transport Models

Viscosity

The molecular model used for the DSMC code is the Variable Hard Sphere (VHS) model of Bird with the parameters given in Ref. 4. The VHS model assumes that the cross section of molecule increases as a function of its energy. The rate of change is related to the coefficient of viscosity. In general, the viscosity coefficient of real gases over a wide temperature range is found to be proportional to the temperature raised to a power of approximately 0.74. The VHS model assumes an isotropic scattering in the center of mass frame of reference. For the simulations presented herein, the viscosity coefficient was modified to better represent the viscosity coefficient in the temperature range of interest (1000-3000 K). The power law viscosity model used for the DSMC simulations is

$$\mu = \left(\frac{T}{T_{ref}} \right)^{0.64} \mu_{ref} \quad (1)$$

where $T_{ref} = 1000$ K and $\mu_{ref} = 3.975 \times 10^{-5}$ Ns/m^2 .

The viscosity law chosen for the Navier-Stokes calculations was Keyes model²¹ for nitrogen. Keyes model takes the following form (in Ns/m^2)

$$\mu = \frac{a_0 \sqrt{T}}{1 + \frac{a}{T \cdot 10^{(a_1/T)}}} \quad (2)$$

where $a_0 = 1.418 \times 10^{-6}$, $a = 116.4$, and $a_1 = 5$, and was correlated for a range of 90 K $< T < 1695$ K.

Viscosity results for the power law and Keyes model are shown in Fig. 1 up to 4000 K. Also given in the figure are Sutherland's law for air and the original power law model with the 0.74 exponent for reference. Up to approximately 2500 K all models show good agreement with the experimental data from Refs. 22-24. The original power law model shows the best agreement between 3000 and 4000 K; however, the slope change evident in the experimental data around 2500 K is due to dissociation of the diatomic nitrogen (this data is for equilibrium dissociated nitrogen at 1×10^5 N/m^2 (1 bar)). In the simulations to be discussed later, chemical nonequilibrium was examined and only trace amounts of atomic nitrogen were found (mass fractions of less than 1×10^{-20}). Therefore, Keyes model and the new power law model are deemed more appropriate for this case.

The error in the viscosity found from the various models relative to the experimental data is presented in Fig. 2. Between 100 K and 2500 K, the error in Keyes model is approximately constant at 1%, while the error in the new power law model is below 6%. The original power law model overpredicts the viscosity by as much as 25% near 2500 K. Since the experimental viscosity data above 3000 K again account for equilibrium dissociation, the error estimates in this range are not valid.

Thermal Conductivity

Keyes model for the thermal conductivity takes the same form as that for the absolute viscosity, however the constants are given as $a_0 = 1.8506 \times 10^{-3}$, $a = 77$, and $a_1 = 12$. Using these constants and the form specified in Eq. (2) gives the thermal conductivity, k (W/mK), calibrated in the range 273 K $< T < 773$ K. A comparison of Keyes model for thermal conductivity with experimental data²²⁻²⁴ indicates that the model does not perform well at higher temperatures (see Fig. 3). Better agreement with the data is found by assuming a power law profile. For the Navier-Stokes code, a power law profile with an exponent of 0.74, $T_{ref} = 1000$ K and $k_{ref} = 0.0631$ W/mK is used and is shown in Fig. 3. The effective thermal conductivity found by using the new power law relation for viscosity and a variable specific heat from the curve fits discussed earlier (used in the DSMC code with the VHS model) is also shown (labeled power law new). Both of the power law models show good agreement with the experimental data below 2000 K. Above 2000 K, the experimental data is again

for equilibrium dissociated nitrogen at $1 \times 10^5 \text{ N/m}^2$ (1 bar) and is therefore not applicable.

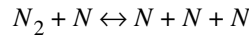
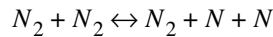
Thermal Nonequilibrium Models

The DSMC code uses the Borgnakke Larsen energy exchange model⁴ with constant rotational relaxation number of 5 and a variable vibrational relaxation number given by the Millikan and White²⁵ formula (see Ref. 4). According to this model and for a fraction of the collisions the total energy is reassigned by sampling from the equilibrium distributions at a temperature that reflects the total collision energy.

The Navier-Stokes code employs the standard Landau-Teller formulation for vibrational relaxation³² and uses the vibrational relaxation time scale for nitrogen suggested by Millikan and White.²⁵ The Millikan and White time scale was originally developed through comparison to shock tube data, and is thus expected to be accurate in the nose region. However, this formulation may not produce accurate vibrational relaxation for strongly expanding flows²⁶ due to anharmonic effects and non-Boltzmann population distributions in the vibrational energy levels.²⁷

Chemical Reaction Model

The chemistry model used in the DSMC code is the Total Collision Energy (TCE) model of Bird.⁴ The TCE model extracts a reaction probability from the Arrhenius reaction rate assuming equilibrium energy distributions. A reduced set of two dissociation reactions of nitrogen was implemented:



The data for the Arrhenius reaction rates was taken from Park.²⁹ The Navier-Stokes code employs the Arrhenius form of the reactions and uses Park's effective temperature $T = \sqrt{TT_v}$.

Flow Conditions and Solution Procedure

Baseline Freestream Conditions

The nominal freestream and surface boundary conditions used for both the Navier-Stokes and DSMC codes are for Case B55D, Run 31 of Ref. 2 and are presented below in Table 1. The fluid is nitrogen, and the thermal nonequilibrium models discussed earlier are used. Since the thermal state at the test section was not specified, the rotational and vibrational temperatures are assumed to be in equilibrium with the translational temperature at 144.44 K for this baseline case. Note that in all of the results presented herein, the axial coordinate x is measured from the virtual nose tip of the sharp fore-cone.

Table 1 Freestream and Boundary Conditions

Mach Number	11.3
Reynolds Number / m	142,060.
Stagnation Temperature, K	3283.
Stagnation Enthalpy, m^2/s^2	3.9670×10^6
Stagnation Pressure, N/m^2	3.6266×10^6
Velocity, m/s	2764.5
Temperature, K	144.44
Static Pressure, N/m^2	21.99
Wall Temperature, K	297.22

The DSMC code uses structured multi-region body fitted grids.⁵ The final baseline grid used in this study consisted of approximately 1 million cells and is presented in Fig. 4. Cell clustering was employed so that most of the cells are clustered between the shock and body. The cell width in the boundary and shock layer area was significantly less than local mean free path.

The Navier-Stokes grids were generated using the Gridgen³¹ grid generator. Three grid levels were used in order to assess the solution accuracy. The finest mesh has 256 cells along the body and 128 cells normal to the surface (Mesh 1). The coarser meshes (Meshes 2 and 3) were determined by eliminating every other mesh point in each direction (i.e., grid halving). When generating the fine mesh, the first 64 cells from the wall were generated by hyperbolically marching the grid from the surface. In the nose region, the initial spacing at the wall was $2.4 \times 10^{-6} m$ and the geometric growth rate was 1.005. On the aft portion of the grid ($x > 0.65 m$), the wall spacing was $8 \times 10^{-6} m$ and the geometric growth rate was 1.0075. The mesh between these two regions, as well as the remaining outer mesh, were generated using Gridgen's elliptic solver. The regions of interest are the conical portions of the body. No effort was made to cluster points in the cylindrical portion of the domain as this region is primarily used to insure that a reasonable outflow boundary condition is applied.

Solution Procedures

The DSMC simulations were initialized by assuming the freestream conditions over the entire flowfield and a local equilibrium distribution sampled to initially populate the computational particle distribution. The DSMC algorithm was then repeatedly performed thousands of times in a time accurate manner until the flowfield achieved a steady behavior. Then thousands of time

steps were performed to obtain an ensemble average of the macroscopic field and surface properties. Approximately 150,000 unsteady and 20,000 steady time samples were performed for the baseline simulation using a fixed time step of 5×10^{-8} s. Approximately 20 million computational particles were simulated; the simulations required 40 hours on a 512 processor IBM SP-2 computer.

An outflow boundary was used for the ‘right-hand’ boundary. This model assumes no particles (mass) are allowed to enter this boundary; this model is appropriate for supersonic flows.

All Navier-Stokes solutions were also initialized by applying the freestream conditions over the entire flow-field domain. The governing equations were then advanced in pseudo-time using a global time step until a steady-state solution was obtained. The CFL (Courant-Friedrichs-Lewy) number at the beginning of the simulations was set to 0.1. This value was then geometrically ramped up by a factor of 1.01 until the maximum CFL number was reached. Although the simulations were stable at CFL numbers as large as 1×10^9 , these large CFL numbers resulted in oscillatory behavior on the finer grids in the form of unsteady vortex shedding from the recirculation regions. The maximum CFL number that allowed convergence was approximately 200 on the 128×64 mesh and 50 on the 256×128 mesh. These CFL numbers correspond to Δt values of roughly 8×10^{-8} s and 1×10^{-8} s, respectively. Due to the CFL limitations, a large number of iterations were needed to obtain steady-state solutions (e.g., 200,000 for the 128×64 mesh and 400,000 for the 256×128 mesh).

The Navier-Stokes code used a zero-gradient, Neumann type outflow boundary.

Simulation Accuracy

DSMC

It is difficult to quantify the simulation error of a DSMC simulation since traditional PDE-based approaches are not appropriate. The method has been shown to be very accurate if the time step is small enough, the cell size is on the order of a local mean-free-path and there are sufficient computational particles per cell to minimize a statistical bias. However, this only addresses the issue of *computational accuracy*; the *physical correctness* of the simulation depends heavily on the type of boundary conditions applied.

Iterative Convergence

The simulations were marched in a time-like manner using a constant time step until the surface quantities, shear stress and heat flux, were statistically invariant. Then the simulation continued with the same time step

and an ensemble average of the macroscopic flow and surface properties were obtained. The fixed time step was less than the mean collisional time step of the flow. Recall that an *outflow boundary condition* was used for the downstream boundary so there was no coupling of the downstream to the upstream flow field.

Grid Convergence

A requirement for an accurate DSMC simulation is that the grid spacing be less than a mean-free-path or the local flow gradient. Three different grids were used in this study: 250,000, 700,000 and 1 million cells. The final grid met the grid spacing criteria from the nose to the compression corner. Approximately 20 million computational particles were simulated on this final grid; the number of particles per cell ranged from 10 to approximately 40 through the domain.

Navier-Stokes

Iterative Convergence

The simulations were marched in pseudo-time until a steady state was reached. A steady state was assumed when the L2 norms of the residuals for the flow equations (mass, momentum, and energy) were reduced by at least ten orders of magnitude; however, in some cases, the norms for the vibrational energy equation leveled out before a ten order of magnitude drop could be achieved. The residual is defined by substituting the current solution into the steady state form of the governing equations (i.e., without the time derivatives). Neglecting machine round-off errors, the residuals will be zero at steady state.

The L2 residual norms for the baseline case are presented in Fig. 6. The residuals for the mass, momentum, and total energy conservation equations show a reduction of more than ten orders of magnitude from their initial levels. However, the residuals for the vibrational energy equation only show a reduction of seven orders of magnitude. The demonstrated iterative convergence gives confidence that the iterative errors in the discrete solution are small and may be neglected relative to the grid convergence errors to be discussed below.

Grid Convergence

Grid (or spatial) convergence has been evaluated by using the steady-state solutions on three meshes, 1, 2, and 3 (from finest to coarsest). The Richardson extrapolation procedure³⁰ has been used to obtain more accurate results from the relation

$$f_{RE} = f_1 + (f_1 - f_2)/3 \quad (3)$$

The above relation assumes that the numerical scheme is second-order, that both mesh levels are in the asymp-

otic grid convergence regime, and that a constant mesh refinement factor of two (i.e., grid doubling) is used. If these assumptions hold, then the Richardson extrapolated results will be third-order accurate since an upwind scheme is used. The accuracy of the surface properties on the three mesh levels has been estimated with the exact solution approximated with f_{RE} which gives the solution error as

$$\% \text{ Error of } f_k = 100(f_k - f_{RE})/f_{RE} \quad (4)$$

where $k=1, 2, 3$ is the mesh level.

If the mesh has been refined sufficiently such that the solution displays a second-order behavior, then the errors on the three meshes will obey the following relationship:

$$\begin{aligned} \% \text{ Error of } f_1 &= \frac{\% \text{ Error of } f_2}{4} \\ &= \frac{\% \text{ Error of } f_3}{16} \end{aligned} \quad (5)$$

In Eq. (5), the first equality will always be satisfied when Eq. (3) is used. The second equality will only be satisfied if all three meshes have been sufficiently refined so as to be in the second-order asymptotic range.

Surface pressure distributions for the three mesh levels are given in Fig. 7 for the Navier-Stokes code. As the grid is refined, both the initial separation point and the pressure peak move forward. The initial separation point is discernible by a sharp rise in pressure above the 25 deg. cone value and occurs at approximately 0.06 m for the fine mesh and 0.08 m for the coarse mesh. The pressure peak is a result of the shock-shock interaction and occurs near 0.1 m for all meshes.

The normalized errors from Eq. (5) are presented in Fig. 8 for the surface pressure. The simulations appear to be grid resolved on all three grid levels upstream of the initial separation point and downstream of the final reattachment point (located at approximately 0.12 m). The fine grid errors upstream of the initial separation point are below 1%, while the fine grid errors downstream of the separated region vary from approximately 2% near the reattachment point, to as high as 15% on the cylindrical portion of the model. Large grid convergence errors on the cylinder were deemed acceptable as the region downstream of the 55 deg.-cylinder juncture is not of interest in this study. Moreover, the errors on the cylindrical portion of the body should have a negligible effect upstream on the regions of interest for the Navier-Stokes simulation. The large spikes in the error are due to the growth of the separated region as the mesh is refined. If the flow at a given location is attached on the medium grid, but separated on the fine

grid, then the Richardson Extrapolation procedure is not appropriate. The errors in the surface pressure within the separated region can be more easily quantified by examining the enlarged view presented in Fig. 9. The errors in this region are below 3%; however, these results should be used with caution since they are not grid refined on all three meshes (i.e., Eq. (5) is not satisfied).

The results for surface heat flux are not as grid resolved as those for surface pressure, as shown in Fig. 10. The heat flux errors in the attached regions are below 1% upstream and 2.5% downstream (again, neglecting the cylindrical region). The errors in the separated regions, however, are as large as 10%. Again, the solutions in the separated regions are not grid converged since Eq. (5) is not satisfied. The 10% error estimates are larger than the quoted uncertainty in the surface heat flux measurements from the experiment and thus suggests the need for further grid refinement. While future work is expected to include an additional refinement level, it will be shown in the next section that the 10% error estimate in heat flux is smaller than the uncertainty in the freestream boundary conditions.

Simulation Results

Baseline Results

This section contains results using the baseline freestream conditions given earlier in Table 1. Streamlines of the separated region, at the 25 deg.-55 deg. juncture, are presented in Fig. 11 for the Navier-Stokes code. The primary vortex is a large, toroidal recirculation zone approximately 0.045 m in length which rotates in a clock-wise direction. A secondary, counter-clock-wise vortex also exists and is approximately 0.01 m long. The size and number of vortices was found to depend strongly on the level of grid refinement for the Navier-Stokes code. The coarse mesh (64×32 cells) had only a single clock-wise vortex which was roughly 0.02 m in length. The flow separates at roughly $x = 0.065 m$, as measured from the effective sharp cone tip. The flow reattaches at approximately $x = 0.11 m$ and remains attached over the remainder of the body.

Figure 15 shows the ratio of translational to rotational temperatures in the flowfield. In a perfect equilibrium case, the ratio should have been unity throughout the domain. The two separate regions with high ratios only indicates area of non-equilibrium. This can be seen in detail in the following figure.

Temperature profiles along the stagnation streamline are shown in Fig. 16 for both the DSMC and Navier-Stokes codes. For the Navier-Stokes code, the shock (denoted by the rise in translational temperature) occurs over a number of grid points. The vibrational tempera-

ture was assumed to be in equilibrium with the translational temperature in the freestream, and achieves a peak value along the stagnation streamline of approximately 475 K. The Millikan and White vibrational relaxation time scale is expected to perform well in this compressive region. The DSMC results show complete non-equilibrium between the translational, rotational, and vibrational modes. A thicker shock is simulated due to the diffusion upstream of high energy molecules. Caution should be used when interpreting the translational temperature upstream of the shock in a DSMC simulation since the scalar translational temperature is determined assuming a Boltzmann distribution; a bimodal distribution can result between the upstream and either surface or shock reflected molecules so the computed scalar translational temperature is not valid.

Figures 17 and 18 compare the surface pressure and heat flux results for the DSMC and NS simulations. The overall agreement is very good; the primary difference is that the NS simulations predict a larger recirculation region than the DSMC results. The difference in the peak surface values in the recirculation region are simply due to the much finer DSMC grid. Since the experimental data consists of surface pressure and heat flux, it is not clear whether these data can resolve the issue of one or two vortices in the recirculation region.

Sensitivity Studies

Minimum and Maximum Energy

In Ref. 3, Holden gives the accuracy of the freestream dynamic pressure and stagnation enthalpy to within $\pm 5\%$ and the Mach number to within $\pm 1.5\%$. In order to examine the sensitivity to the freestream properties, the stagnation enthalpy was varied by the suggested $\pm 5\%$. The stagnation enthalpy was chosen so as to effectively yield the minimum and maximum energy limits. At the test section location, the stagnation or total enthalpy can be separated into two parts, a sensible enthalpy and a kinetic energy term. Due to the low static temperature and high velocity, nearly all of the energy is in the form of directed kinetic energy (i.e., velocity squared). To simplify the determination of boundary conditions for the codes, and since the true thermodynamic state at the test section is unknown, the freestream axial velocity was simply varied by $\pm 2.5\%$ since $V \propto \sqrt{H_o}$. The resulting freestream velocities are 2695.5 m/s (minimum energy) and 2833.5 m/s (maximum energy).

Vibrationally Excited Flow

An additional uncertainty in the boundary conditions is the vibrational excitation state at the test section.³³ The vibrational state in the tunnel is not addressed in the

experimental description.^{2,3} The minimum amount of vibrational excitation is found by assuming thermal equilibrium in the test section, i.e., the vibrational temperature is equal to the translational temperature (144.44 K). This value was used in the baseline freestream conditions. The maximum possible vibrational excitation level would occur if the vibrational temperature was frozen at the stagnation temperature in the test section (3283.3 K). In order to maintain the baseline total enthalpy at the test section, the axial velocity was also reduced to 2403.8 m/s.

This maximum vibrational excitation level could occur if, in the driven section of the tunnel, the fluid behind the reflected shock wave has sufficient flow residence time to thermally equilibrate at the stagnation temperature. Then, as the driven gas expands through the nozzle throat, the expansion ratio is sufficiently large enough that the vibrational temperature freezes out near the stagnation temperature. While the true state in the tunnel is somewhere in between these two limits, the experience of the authors with some hypersonic expanding flows suggests that the vibrational temperature could be closer to the stagnation temperature than to the translational temperature at the test section.

The Millikan and White vibrational relaxation time scale has been shown to overpredict the vibrational relaxation times for strongly expanding flows. Ruffin^{27,28} discusses how the Millikan and White relaxation time (τ_{MW}) may be modified by an acceleration factor ϕ for expanding flows as follows:

$$\tau_{vib} = \tau_{MW}/\phi \quad (6)$$

Ruffin suggests that ϕ is a function of the translational temperature T and the T_v/T ratio only. For the baseline case, the T_v/T ratio is less than or equal to unity, suggesting that the Millikan and White time scale is valid. For the vibrationally excited case, the T_v/T ratio is less than two, giving maximum ϕ values near 1.5; thus, the Millikan and White relaxation time scale should still be a good approximation for the vibrational relaxation. See Refs. 19, 27, and 28 for more details.

Sensitivity Results

Three additional cases were run with the DSMC and Navier-Stokes codes: a minimum energy case, a maximum energy case, and a vibrationally excited case where the baseline energy (i.e., total enthalpy) was assumed. The sensitivity of the surface pressure to the freestream uncertainties is shown in Fig. 19 for the Navier-Stokes code. The surface pressures are lower than the baseline for the minimum energy case, especially in the separated region. The opposite is true for the maximum energy case. The vibrationally excited case resulted in significantly lower pressure values over

the conical surfaces due to significant flow energy being tied up in the vibrational modes. These results are quantified in Fig. 21, where the percent difference between the baseline case and the additional flow cases are shown according to the following relation:

$$\% \text{ Difference} = \frac{P - P_{\text{baseline}}}{P_{\text{baseline}}} \times 100 \quad (7)$$

Large increases in the percent difference occur when the flow features (e.g., separated region, shock-shock intersection) move along the surface. In general, the minimum and maximum energy cases ($\pm 5\%$) result in a sensitivity of $\pm 5\%$ in the surface pressure. For the vibrationally excited case, the surface pressures are 25% lower than those found in the baseline case. These results suggest that the largest uncertainty in the experimental data is due to a lack of knowledge of the vibrational excitation levels at the test section.

The sensitivity of the surface heat flux to the uncertainties in the freestream properties is shown in Fig. 23 for the Navier-Stokes code. Again, the minimum and maximum energy cases result in a reduction and increase in the surface heating, respectively. The vibrationally excited case results in heating levels well below the baseline case. These sensitivities are quantified in Fig. 25, which gives the percent difference in surface heat flux between the various cases and the baseline simulation. The minimum and maximum energy cases result in heating levels of minus/plus 8%, respectively. The effects of vibrational excitation are to lower the heating by 25%-35% below the baseline results. Again, uncertainty in the vibrational excitation state is the largest contributor to the overall uncertainty in the experimental data.

Figures 22, 24, and 26 show the similar sensitivity results for the DSMC simulations. Again, the DSMC and NS results compare quite well except that the recirculation zone is predicted to be much larger for the NS simulations.

The DSMC simulations did not predict any statistically significant chemical activity in the flow. The real gas effects therefore were limited to vibrational and rotational non-equilibrium.

Conclusions

Simulations were performed using DSMC and Navier-Stokes codes for the laminar Mach 11 flow of nitrogen over a blunted 25 deg.-55 deg. biconic. The flowfields obtained were such that significant regions of attached flow were found both upstream and downstream of the cone-cone juncture separated region. The simulations accounted for both thermal and chemical nonequilibrium. While significant amounts of thermal

nonequilibrium were observed in the flowfield, the amount of dissociation was found to be negligible. Surface pressure and heating results for the baseline freestream conditions showed good agreement between the DSMC and Navier-Stokes approaches with the exception that the recirculation zone was predicted to be larger for the NS simulation.

The DSMC simulations were performed to achieve the grid spacing, time step, and cell particle population constraints over the domain of interest (from the nose to the compression flare). The viscosity coefficient and reference diameter were changed to accurately represent the nitrogen viscosity in the temperature range of interest.

The accuracy of the Navier-Stokes simulations was examined. The iterative convergence was demonstrated by obtaining a ten order of magnitude drop in the L2 norm of the residuals. Estimates of the grid convergence error were obtained by applying the Richardson Extrapolation procedure using two mesh levels. A third grid level was used to determine if the solutions were in the asymptotic second-order grid convergence range. The surface quantities were found to be grid converged in the attached portions of the flow, but not in the separated regions. The grid convergence errors were found to be below 2.5% in the attached flow regions for both surface pressure and heat flux. Errors in the separated region were estimated to be as high as 3% for surface pressure and 10% for the surface heat flux.

The sensitivity of the surface properties to uncertainties in the freestream conditions was examined. Two additional cases were run which represented minimum and maximum total energy cases according to the quoted experimental uncertainties in stagnation enthalpy ($\pm 5\%$). The minimum energy case resulted in surface pressures 5% below and surface heat fluxes 8% below the baseline values, while the maximum energy case resulted in surface pressures and heat fluxes 5% and 8% above the baseline values, respectively. The baseline case assumed that the vibrational energy modes in the freestream were in equilibrium with the translation modes. An additional case was run in which the vibrational temperature in the freestream was assumed to be frozen at the stagnation temperature, but the total energy level was held constant at the baseline energy. This vibrationally excited case generally resulted in surface pressures 25% lower than the baseline case. The surface heat fluxes for this case were 25%-35% lower than the baseline heating values. Thus, the sensitivities of the surface properties to uncertainties in the vibrational excitation state at the test section far outweigh the uncertainties in the surface measurements³ themselves ($\pm 3\%$ for surface pressure and $\pm 5\%$ for heat flux) and the estimated errors in the simulations ($\pm 3\%$ for surface pressure and $\pm 10\%$ for

heat flux). In light of the findings of this sensitivity study, we recommend that the vibrational state at the test section be examined.

The primary differences between the NS and DSMC results, the size of the recirculation region and the number of vortices, remain unresolved at this time. The experimental data may indicate the vortex size; however, the number and structure of the recirculation zone would require surface shear and possibly flowfield measurements. The authors believe that the difference could be either due to differences in modelling the outflow boundary or non-equilibrium effects in the nose region (see figure 16). For the outflow boundary, a zero-gradient model is used in the NS simulations and a non-reentrant boundary used in the DSMC simulations. Since the outflow will be subsonic to mildly sonic in a portion of this boundary, the boundary condition in the DSMC simulations may be the cause of the difference in the recirculation zones. The non-equilibrium effects of the nose region may be investigated by taking the DSMC solution of the nose region as a upstream boundary for the Navier-Stokes simulation. These will be topics for future investigations.

Acknowledgments

The authors would like to thank Dr. Michael Holden of Calspan-UB Research Center for providing the experimental data. We would also like to thank Dr. Basil Hassan and Dr. Steven Beresh of Sandia National Laboratories for their reviews of this paper.

References

1. *Guide for the Verification and Validation of Computational Fluid Dynamics Simulations*, AIAA G-077-1998, p. 3.
2. "Experimental Database from CUBRC Studies in Hypersonic Laminar and Turbulent Interacting Flows Including Flowfield Chemistry," prepared for RTO Code Validation of DSMC and Navier-Stokes Code Validation Studies, Calspan-University at Buffalo Research Center, Buffalo, NY, June 2000.
3. M. Holden, "Experimental Studies of Laminar Separated Flows Induced by Shock Wave/Boundary Layer and Shock/Shock Interaction in Hypersonic Flows for CFD Validation," AIAA Paper 2000-0930, Jan. 2000.
4. G. A. Bird, *Molecular Gas Dynamics and the Direct Simulation of Gas Flows* (Oxford University Press, Oxford, 1994).
5. T. J. Bartel, S. J. Plimpton, J. E. Johannes, and J. L. Payne, "Icarus: A 2D Direct Simulation Monte Carlo (DSMC) Code for Parallel Computers," Sandia Report SAND 96-0591, Sandia National Laboratories, Albuquerque, New Mexico, 1997.
6. C. C. Wong, F. G. Blottner, J. L. Payne, and M. Soetrisno, "Implementation of a Parallel Algorithm for Thermo-Chemical Nonequilibrium Flow Solutions," AIAA Paper 95-0152, Jan. 1995.
7. Wong, C. C., Soetrisno, M., Blottner, F. G., Imlay, S. T., and Payne, J. L., "PINCA: A Scalable Parallel Program for Compressible Gas Dynamics with Non-equilibrium Chemistry," SAND 94-2436, Sandia National Laboratories, Albuquerque, NM, 1995.
8. INCA User's Manual, Version 2.0, Amtec Engineering, Inc., Bellevue, WA, 1995.
9. Steger, J. L., and Warming, R. F., "Flux Vector Splitting of the Inviscid Gasdynamic Equations with Applications to Finite Difference Methods," *Journal of Computational Physics*, Vol. 40, 1981, pp. 263-293.
10. Van Leer, B., "Towards the Ultimate Conservative Difference Scheme. V. A Second Order Sequel to Godunov's Method," *Journal of Computational Physics*, Vol. 32, No. 1, 1979, pp. 101-136.
11. Yoon, S., and Jameson, A., "An LU-SSOR Scheme for the Euler and Navier-Stokes Equations," AIAA Paper 87-0600, Jan. 1988.
12. Yoon, S., and Kwak, D., "Artificial Dissipation Models for Hypersonic External Flow," AIAA Paper 88-3708, 1988.
13. Peery, K. M., and Imlay, S. T., "An Efficient Implicit Method for Solving Viscous Multi-Stream Nozzle/Afterbody Flow Fields," AIAA Paper 86-1380, June 1986.
14. Payne, J. L., and Hassan, B., "Massively Parallel Computational Fluid Dynamics Calculations for Aerodynamics and Aerothermodynamics Applications," Proceedings of the 1998 HPCCP/CAS Workshop, NASA/CP-1999-208757, Jan. 1999, pp. 111-116.
15. B. Hassan, D. W. Kuntz, and D. L. Potter, "Coupled Fluid/Thermal Prediction of Ablating Hypersonic Vehicles," AIAA Paper No. 98-0168, Jan. 1998.
16. D. W. Kuntz, B. Hassan, and D. L. Potter, "An Iterative Approach for Coupling Fluid/Thermal Predictions of Ablating Hypersonic Vehicles," AIAA Paper 99-3460, June-July 1999.
17. Roy, C. J. and Blottner, F. G., "Assessment of One- and Two-Equation Turbulence Models for Hypersonic Transitional Flows," AIAA Paper 2000-0132, January 2000.
18. Roy, C. J., and Blottner, F. G., "Assessment of One- and Two-Equation Turbulence Models for Hypersonic Transitional Flows," to appear in the *Journal of Spacecraft and Rockets*, October 2000.
19. C. J. Roy, M. A. McWherter-Payne, and W. L. Oberkampf, "Verification and Validation for Laminar Hypersonic Flowfields," AIAA Paper 2000-2550, June 2000.
20. McBride, B. J., Gordon, S., and Reno, M. A., "Coefficients for Calculating Thermodynamic and Transport Properties of Individual Species," NASA TM 4513, Oct. 1993.
21. Keyes, F. G., "A Summary of Viscosity and Heat-Conduction Data for He, A, H₂, O₂, CO, CO₂,

Figures

H₂O, and Air,” Transactions of the ASME, July 1951, pp. 589-596.

22. Incropera, F. P., and DeWitt, D. P., *Fundamentals of Heat and Mass Transfer, 3rd Ed.*, Wiley, New York, 1990, p. A18.

23. *CRC Handbook of Chemistry and Physics*, Robert C. Weast, Editor, CRC Press, Florida, 1984, pp. B-363 and E-3.

24. Vargaftik, N. B., “Tables on the Thermophysical Properties of Liquids and Gases In Normal and Dissociated States,” John Wiley and Sons, Inc., New York, 1975.

25. Millikan, R. C., and White, D. R., “Systematics of Vibrational Relaxation,” *Journal of Chemical Physics*, Vol. 39, No. 12, 1963, pp. 3209-3213.

26. Bray, K. N. C., “Chemical and Vibrational Non-equilibrium in Nozzle Flows,” *Nonequilibrium Flows, Part II*, Marcel Dekker, Inc., New York, 1970, pp. 67-68.

27. Ruffin, S. M., “Prediction of Vibrational Relaxation in Hypersonic Expanding Flows Part 1: Model Development,” *Journal of Thermophysics and Heat Transfer*, Vol. 9, No. 3, 1995, pp. 432-437.

28. Ruffin, S. M., “Prediction of Vibrational Relaxation in Hypersonic Expanding Flows Part 2: Results,” *Journal of Thermophysics and Heat Transfer*, Vol. 9, No. 3, 1995, pp. 438-445.

29. C. Park, *Nonequilibrium Hypersonic Aerothermodynamics*, Wiley, New York, 1990.

30. P. Roache, “Ch. 3: A Methodology for Accuracy Verification of Codes: the Method of Manufactured Solutions,” *Verification and Validation in Computational Science and Engineering*, Hermosa Publishers, New Mexico, 1998.

31. Gridgen User’s Manual, Pointwise, Inc.

32. W. G. Vincenti, and C. H. Kruger, Jr., *Introduction to Physical Gas Dynamics*, Wiley, New York, 1975.

33. Personal Communication, Michael Holden, December 6, 2000.

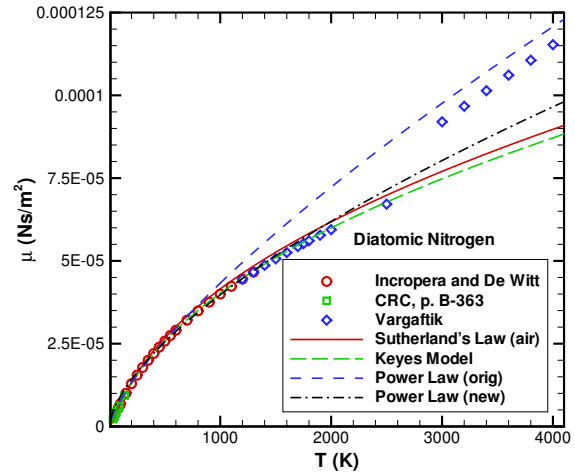


Fig. 1: Comparison of viscosity models to experimental data.²²⁻²⁴

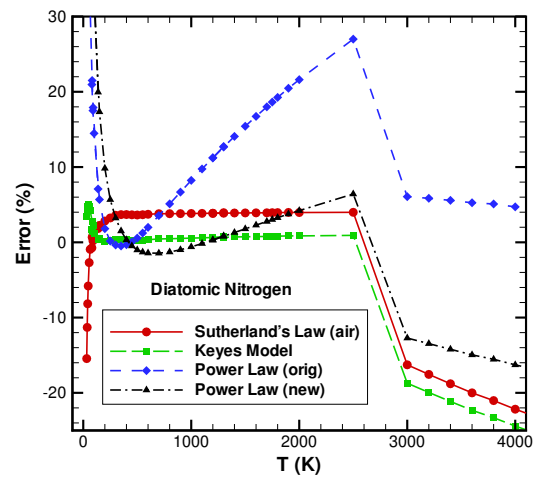


Fig. 2: Error in viscosity models compared to experimental data.²²⁻²⁴

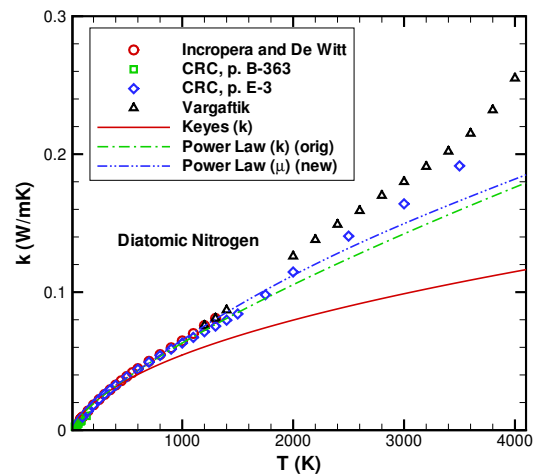


Fig. 3: Comparison of thermal conductivity models to experimental data.²²⁻²⁴

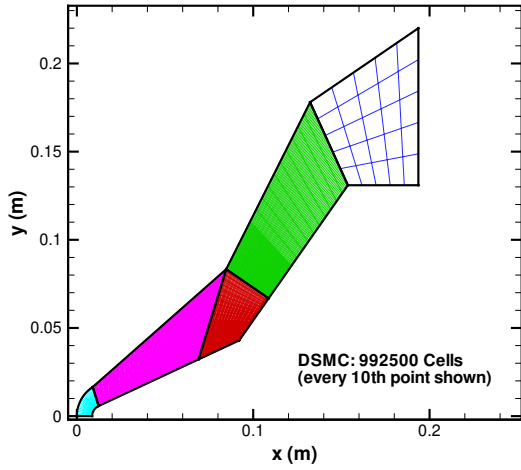


Fig. 4: Flowfield grid for the DSMC simulations.

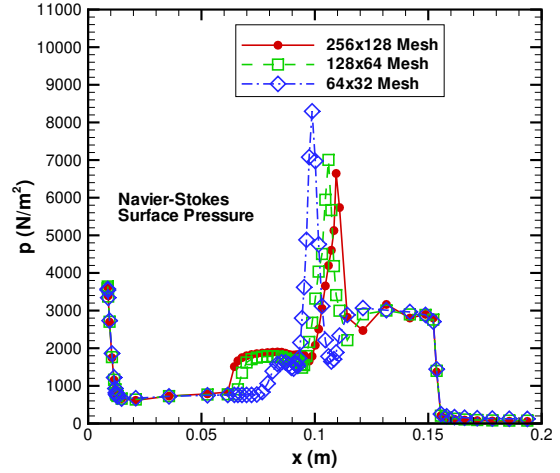


Fig. 7: Surface pressure distributions for three mesh levels (Navier-Stokes).

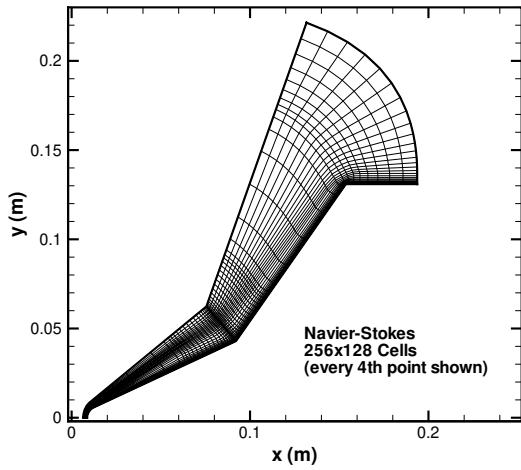


Fig. 5: Flowfield grid for the Navier-Stokes simulations.

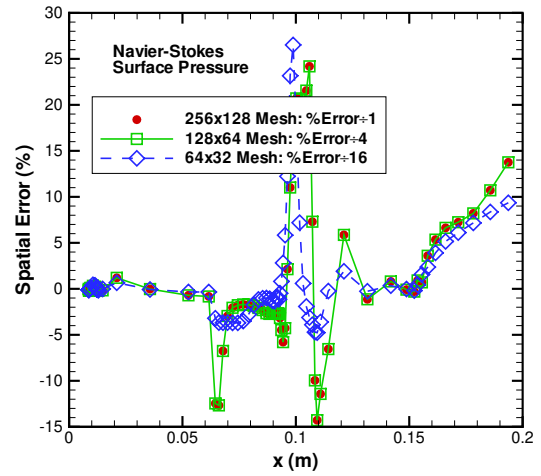


Fig. 8: Spatial error in the surface pressure distributions (Navier-Stokes).

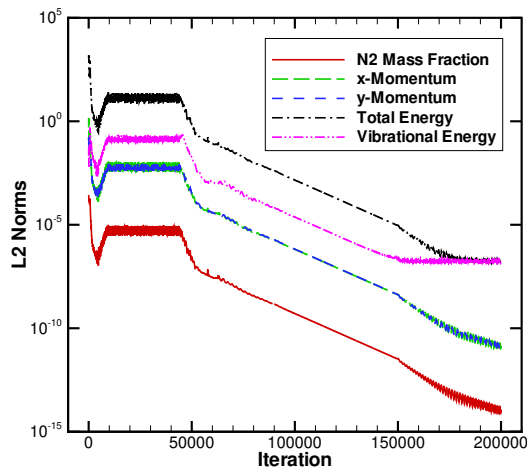


Fig. 6: Iterative convergence of the Navier-Stokes code (128x64 cells).

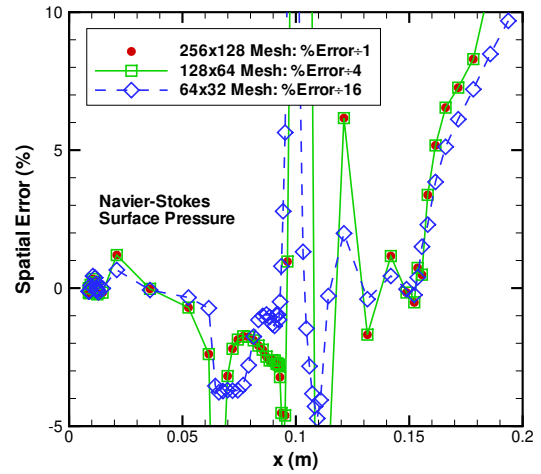


Fig. 9: Spatial error in the surface pressure distributions - enlarged view (Navier-Stokes).

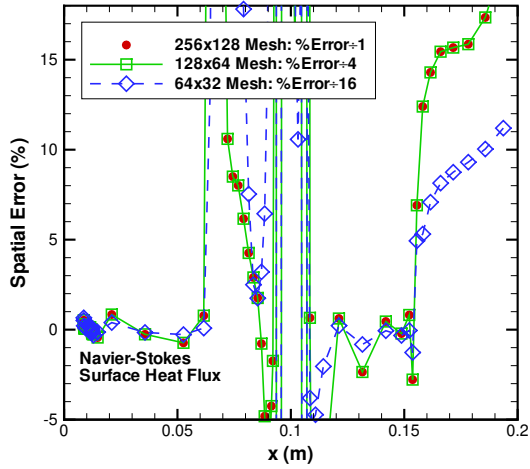


Fig. 10: Spatial error in the surface heating distributions (Navier-Stokes).

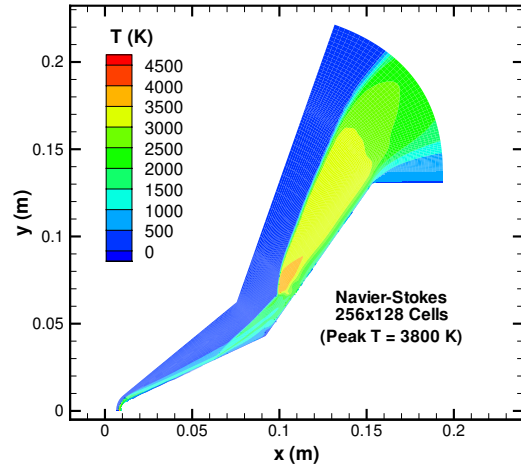


Fig. 13: Contour plot of the translational temperature (Navier-Stokes).

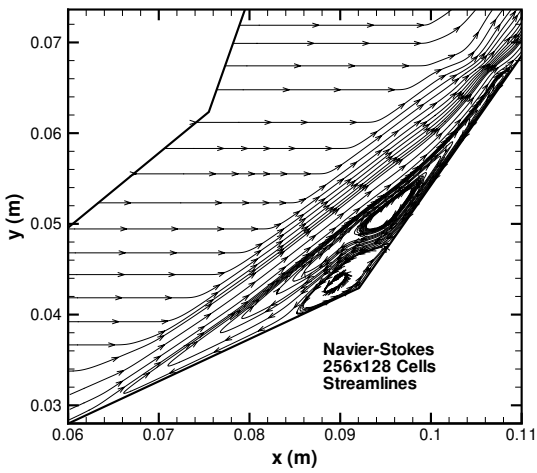


Fig. 11: Streamlines in the separated region (Navier-Stokes).

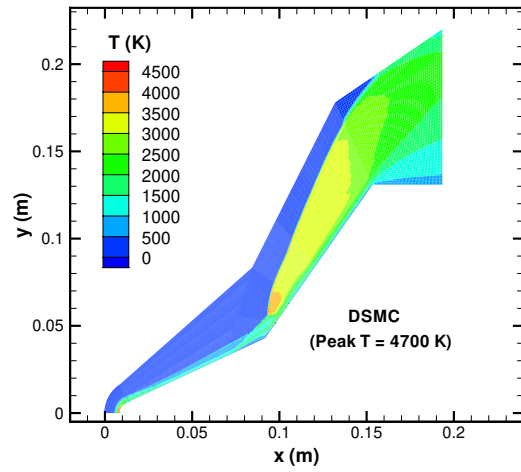


Fig. 14: Contour plot of the translational temperature (DSMC).

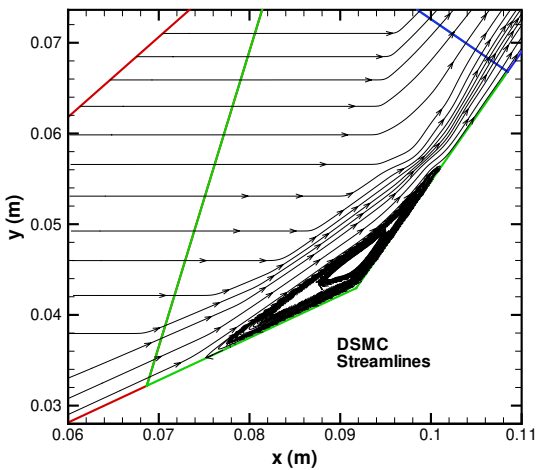


Fig. 12: Streamlines in the separated region (DSMC).

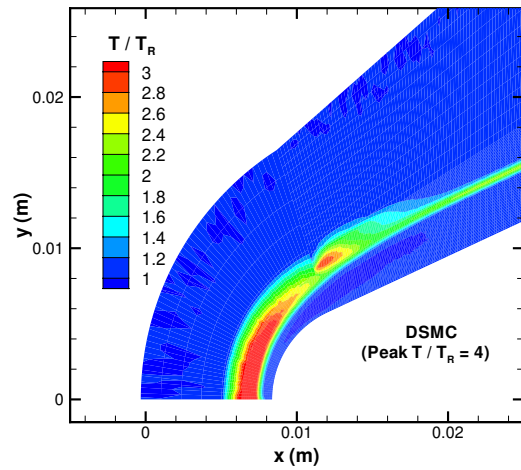


Fig. 15: Contour plot of the translational to rotational temperature ratio (DSMC).

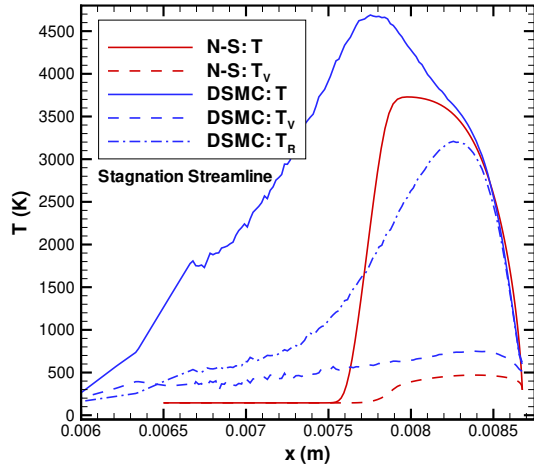


Fig. 16: Temperature profiles along the stagnation streamline (Navier-Stokes in red and DSMC in blue).

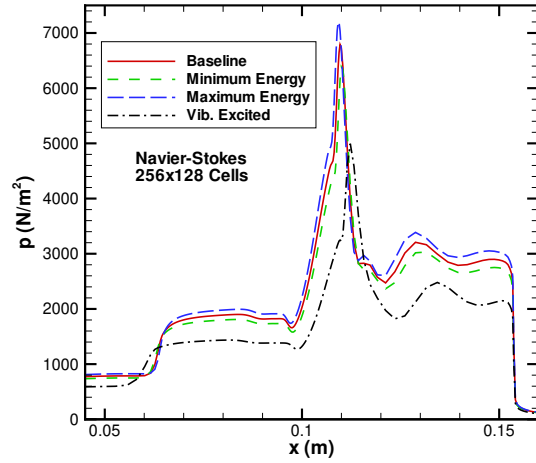


Fig. 19: Sensitivity of the surface pressure to uncertainties in the freestream properties (Navier-Stokes).

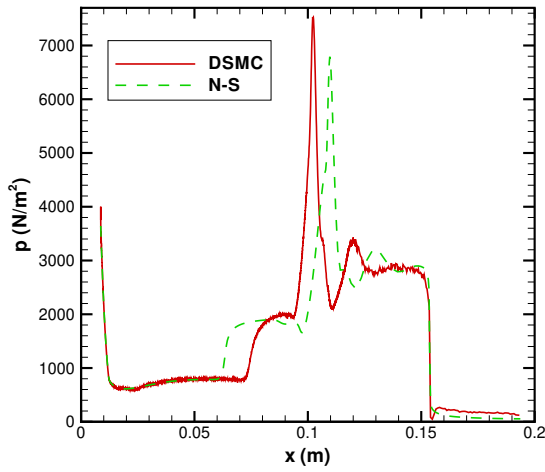


Fig. 17: Baseline surface pressure distributions for the DSMC and Navier-Stokes codes.

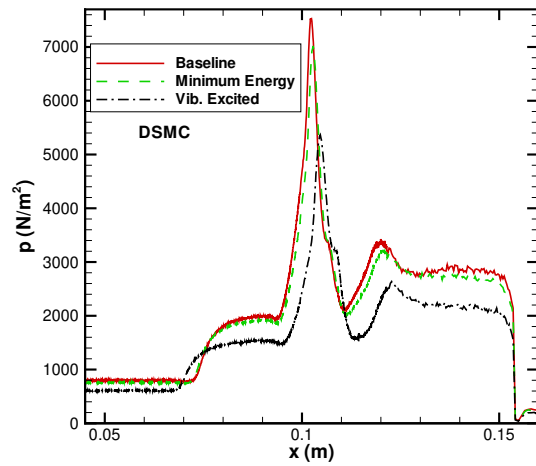


Fig. 20: Sensitivity of the surface pressure to uncertainties in the freestream properties (DSMC).

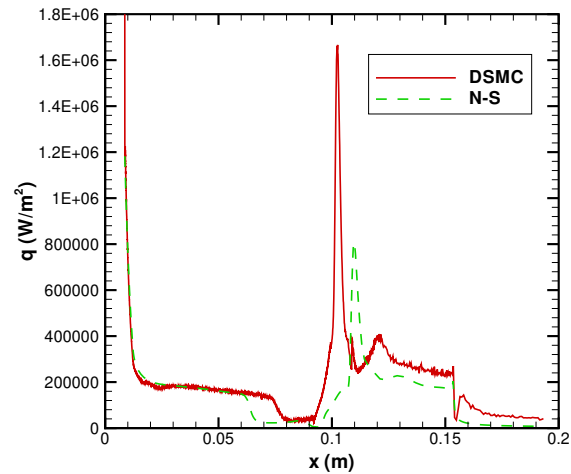


Fig. 18: Baseline surface heat flux distributions for the DSMC and Navier-Stokes codes.

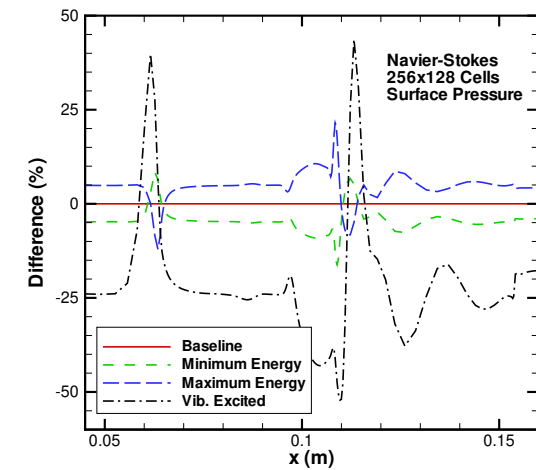


Fig. 21: Differences in surface pressure due to uncertainties in the freestream properties (Navier-Stokes).

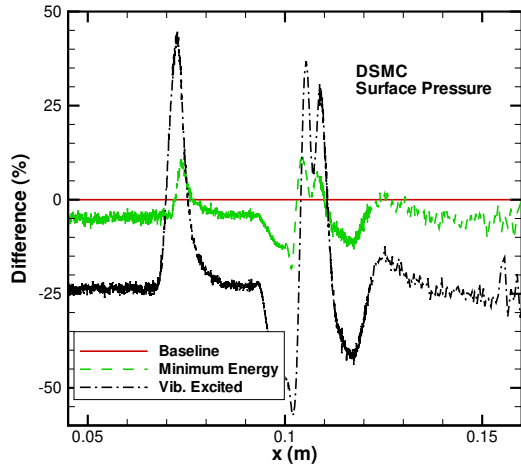


Fig. 22: Differences in surface pressure due to uncertainties in the freestream properties (DSMC).

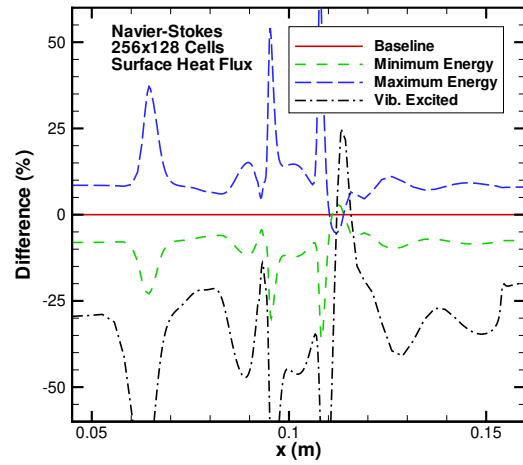


Fig. 25: Differences in surface heat flux due to uncertainties in the freestream properties (Navier-Stokes).

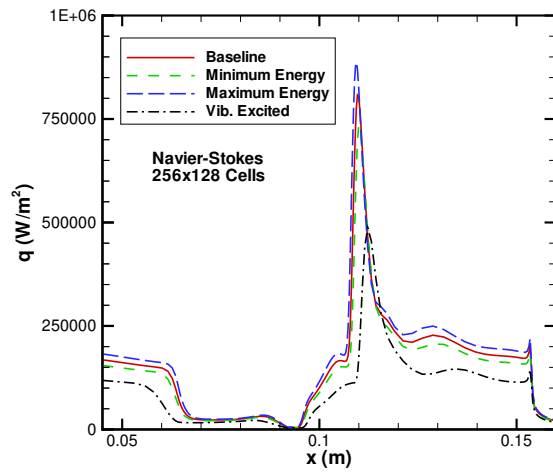


Fig. 23: Sensitivity of the surface heat flux to uncertainties in the freestream properties (Navier-Stokes).

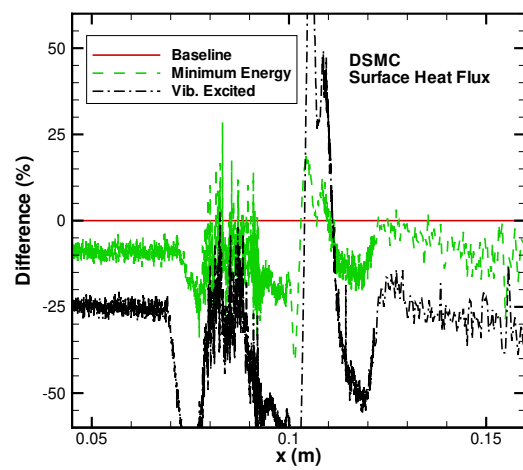


Fig. 26: Differences in surface heat flux due to uncertainties in the freestream properties (DSMC).

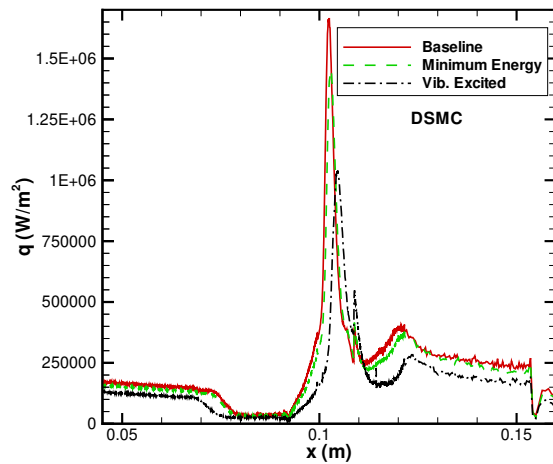


Fig. 24: Sensitivity of the surface heat flux to uncertainties in the freestream properties (DSMC).